

# Temperature gradients in XMM-Newton observed REFLEX-DXL galaxy clusters at $z \sim 0.3$ \*

Y.-Y. Zhang<sup>1</sup>, A. Finoguenov<sup>1</sup>, H. Böhringer<sup>1</sup>, Y. Ikebe<sup>1,2</sup>, K. Matsushita<sup>1,3</sup>, and P. Schuecker<sup>1</sup>

<sup>1</sup> Max-Planck-Institut für extraterrestrische Physik, Giessenbachstraße, 85748 Garching, Germany

<sup>2</sup> Joint Center for Astrophysics, University of Maryland, Baltimore County, 1000 Hilltop Circle, Baltimore, MD 21250, USA

<sup>3</sup> Tokyo University of Science, Tokyo, Japan

Received 5 June 2003 / accepted 22 September 2003

**Abstract.** We present XMM-Newton results on the temperature profiles of a volume-limited sample of galaxy clusters at redshifts  $z \sim 0.3$ , selected from the REFLEX survey (REFLEX-DXL sample). In the spectral analysis, where only the energies above 1 keV were considered, we obtained consistent results on the temperature derived from the pn, MOS1 and MOS2 data. Useful temperature measurements could be performed out to radii with overdensity 500 ( $r_{500}$ ) for all nine clusters. We discovered a diversity in the temperature gradients at the outer cluster radii with examples of both flat and strongly decreasing profiles. Using the total mass and the gas mass profiles for the cluster RXCJ0307.0–2840 we demonstrate that the errors on the mass estimates for the REFLEX-DXL clusters are within 25% up to  $r_{500}$ .

**Key words.** cosmology: observations – galaxies: clusters: general – X-rays: galaxies: clusters

## 1. Introduction

The number density of galaxy clusters probes the cosmic evolution of large-scale structure (LSS) and thus provides an effective test of cosmological models. It is sensitive to the matter density ( $\Omega_m$ ) and the amplitude of the cosmic power spectra on cluster scale ( $\sigma_8$ ) (e.g. Schuecker et al. 2003). Its evolution is sensitive to the dark energy ( $\Omega_\Lambda$ ) (e.g. Vikhlinin et al. 2002). The most massive clusters are especially important in tracing LSS evolution since they are expected to show the largest evolutionary effects. In addition, the X-ray properties of the most massive clusters should be easier to describe in hierarchical modeling since the structure of the X-ray emitting intracluster plasma is essentially determined by gravitational effects and shock heating. With decreasing cluster mass and intracluster medium (ICM) temperature, non-gravitational effects play an important role before and after the shock heating (Voit & Bryan 2001; Voit et al. 2002; Zhang & Wu 2003; Ponman et al. 2003). Therefore, the most massive

clusters provide the cleanest results in comparing theory with observations.

In this project we are analysing an almost volume-complete sample of thirteen X-ray luminous ( $L_X \geq 10^{45}$  erg s<sup>-1</sup> for 0.1 – 2.4 keV) clusters selected from the ROSAT-ESO Flux-Limited X-ray (REFLEX) galaxy cluster survey (Böhringer et al. 2001a) in the redshift interval  $z = 0.27$  to 0.31. There is only a very small correction to the volume completeness with a well known selection function for  $L_X \geq 10^{45}$  erg s<sup>-1</sup> at the higher redshift as described in Böhringer et al. (2003; Paper I). With this REFLEX-DXL (Distant X-ray Luminous) sample we want to obtain a robust measure of the cluster abundance of this epoch, in particular to perform studies of the evolution of the cluster population by comparing these observations with more nearby and more distant clusters. A prime goal is to obtain reliable ICM temperatures of these clusters as a measure of the cluster masses (e.g. Evrard 1997). Since peculiarities in the cluster structure introduce a scatter in the mass–temperature relation and since in particular on-going cluster mergers can lead to a temporary increase in the cluster temperature and X-ray luminosity (Randall et al. 2002), we aim for a detailed study of the deep XMM-Newton observations described here. The clusters are also scheduled for a detailed spectroscopic study

Send offprint requests to: Y.-Y. Zhang,  
e-mail: yzhang@mpe.mpg.de

\* This work is based on observations made with the XMM-Newton, an ESA science mission with instruments and contributions directly funded by ESA member states and the USA (NASA).

**Table 1.** Compilation of some observational information on the nine REFLEX-DXL clusters. Col. (1): Cluster name. Cols. (2–3): Sky coordinates. Cols. (4–6): Net exposure time of MOS1, MOS2 and pn after cleaning for the flaring episodes. Cols. (7–9): Light curve cleaning upper limit. Col. (10): Hydrogen column density in units of  $10^{20}\text{cm}^{-2}$  (Dickey & Lockman 1990). Col. (11): Revolution of XMM-Newton. Col. (12): Alternative name

Cluster (RXCJ)	$\alpha$ ( $^{\circ}$ )	$\delta$ ( $^{\circ}$ )	Exposure Time (s)			Criteria (cts/100s)			$n_{\text{H}}$	orbit	Alternative name
	Eq. J2000.0	MOS1	MOS2	pn	MOS1	MOS2	pn				
0014.3 – 3022	3.5837	–30.3757	15085	15510	10057	23.4	23.7	61.2	1.60	270	A2744 (AC118)
0043.4 – 2037	10.8508	–20.6225	11253	11248	6318	23.5	25.0	69.8	1.54	380	A2813
0232.2 – 4420	38.0717	–44.3453	11979	11508	7741	22.2	22.4	63.4	2.49	474	
0307.0 – 2840	46.7667	–28.6708	12309	12610	8126	21.9	22.5	56.8	1.36	218	A3088
0528.9 – 3927	82.2342	–39.4636	7097	6806	3297	23.3	23.2	57.4	2.13	324	
0532.9 – 3701	83.2350	–37.0260	10374	11191	6527	23.3	25.3	63.0	2.90	518	
0658.5 – 5556	104.5700	–55.9600	25339	23365	18307	24.7	23.6	57.7	6.53	159	1ES0657-558
1131.9 – 1955	172.9858	–19.9258	11660	11164	8511	22.3	22.3	57.8	4.50	286	A1300
2337.6 + 0016	354.4204	0.2760	12216	11915	7412	22.4	23.3	69.1	3.82	365	A2631

of the cluster dynamics with the ESO-VLT-VIMOS instrument.

The selection of the REFLEX-DXL sample and its properties are described in detail in Paper I. For all clusters in this sample the XMM-Newton observations have confirmed that the X-ray luminosity is dominated by diffuse thermal emission from the ICM of these systems. Therefore, the REFLEX-DXL sample contributes a unique sample of X-ray luminous and consequently very massive clusters from roughly the same epoch, which are not only interesting as cosmological probes, but also for astrophysical studies like the statistics of cluster substructure, galaxy evolution, Sunyaev-Zel’dovich observations and many other applications (e.g. Böhringer et al. 2001b).

The estimate or derivation of the cluster mass is an essential step in almost all these studies. The mass can be either approximately estimated from the temperature (Evrard 1997), or determined from the temperature and density distributions of the ICM under the assumption of hydrostatic equilibrium of the intracluster gas (e.g. Cavaliere & Fusco-Femiano 1976; Serio et al. 1981), or otherwise determined from the mass of the intracluster gas and the assumption of the universality of the cluster baryon fraction (e.g. White et al. 1993; Vikhlinin et al. 2002). The first two methods require a robust determination of the ICM temperature and a good understanding of the cluster structure for a reliable interpretation of the results.

Therefore, it is the aim of this paper to establish a reliable method of spatially resolved temperature determination for the clusters in the REFLEX-DXL sample and to derive temperature profiles for all the clusters. XMM-Newton with its superior sensitivity combined with its good spatial resolution provides the best means for such studies (Arnaud et al. 2002). Previously, large data sets on cluster temperature profiles have been compiled from ASCA (e.g. Markevitch et al. 1998; White 2000; Finoguenov et al. 2001a; Finoguenov et al.

2002; Sanderson et al. 2003) and BeppoSAX observations (Molendi & De Grandi 1999; Ettori et al. 2002).

This paper is structured as follows. In Sect. 2, we describe the background components, which are important to this study. Then we present a double background subtraction method, which is developed to provide a precise background removal. In Sect. 3, we analyse the properties of the hot gas in the galaxy clusters, and show our analytic temperature model. Then we determine the total mass and gas mass fraction in the cluster RXCJ0307.0–2840 based on the precise temperature and gas density profiles. In Sect. 4, we draw our conclusions. We adopt a flat  $\Lambda$ CDM cosmology with the density parameter  $\Omega_{\text{m}} = 0.3$  and the Hubble constant  $H_0 = 70 \text{ km s}^{-1} \text{ Mpc}^{-1}$ . Error bars correspond to the 68% confidence level, unless explicitly stated otherwise.

## 2. Method

### 2.1. Data preparation

Of the thirteen XMM-Newton observations of REFLEX-DXL clusters conducted so far, eight have sufficient quality for the detailed studies described here. The remaining five clusters are heavily affected by soft proton flares. Some properties of these observations are described in Paper I. Re-observations of these targets have been allocated. An additional X-ray luminous REFLEX cluster RXCJ0307.0–2840 at  $z = 0.2578$  was observed in this project and is also analysed here. It has very good observational data and appears to be a very regular and symmetric cluster. We have therefore selected this object as an example to demonstrate our method of analysis.

An overview on the observational data of the complete sample of thirteen plus one clusters is given in Paper I. In this paper we compiled further observational information on the sample targets in Table 1, which includes the observational parameters of the data and the alternative names of these targets.

We use the XMMSAS v5.4 software for data reduction. The MOS and pn data were taken in standard Full Frame mode and Extended Full Frame mode, respectively. For all detectors, the thin filter has been used.

Above 10 keV, there is little X-ray emission from the clusters due to the low telescope efficiency at these energies; the particle background therefore completely dominates. The cluster emission is not variable, so any spectral range can be used for temporal variability studies of the background. Therefore, the 10–15 keV energy band (binned in 100 s intervals) was used to monitor the particle background and to excise periods of high particle flux. In this screening process we use the settings  $FLAG = 0$  and  $PATTERN < 5$  for pn, and  $PATTERN < 13$  for MOS. As an example, Fig. 1 shows the 10–15 keV pn light curve of RXCJ0658.5–5556.

We reject those time intervals affected by flares in which the detector countrate (ctr) exceeds a threshold of  $2\sigma$  above the average ctr, where the average and the variance have been interactively determined from the ctr histogram below the rejection threshold. A similar cleaning criterion is applied to the screening of the background observation. We note, however, that the thresholds will be different for the source and background accumulations. Formal freezing of the cleaning criterion does not overcome the difference in the mean background ctr. In our analysis we searched through a number of background observations to find the one matching our target observations. The selection criterion is therefore to find the one with a similar cleaning threshold.

As shown in Table 1, the pn and MOS detectors all have their own similar cleaning thresholds for all observations. In Sect. 2.2 we consider in detail how this background behaviour affects the temperature determination.

In the analysis of the pn data, we statistically remove the out-of-time effect by creating an out-of-time (OOT)

event list file and using the XMMSAS products such as images and spectra to subtract it. The present observations have been taken in the Extended Full Frame mode (frame time=199 ms). **At this mode, the fraction of OOT effect amounts 2.32%, which we used to normalize the XMMSAS OOT product before we subtract it from the XMMSAS normal product.**

## 2.2. Background analysis

The purpose of the background analysis described in the following is to find a suitable “blank field” observation to be used for the background subtraction and to further analyse the difference between the target and background to take this residual background into account.

The background has several components which exhibit different spectral and temporal characteristics. In the low energy band ( $< 0.3$  keV), the instrumental background is dominated by electronic noise consisting of a large number of small amplitude events added up during each frame accumulation (Read 2002). This noise depends on the read-out frequency of the cameras and is sensitive to the energy offset of each individual pixel. Energetic particles produce several line and continuum components in the background, which can be further subdivided into time variable and constant components. The constant component has been intensively studied by Lumb et al. (2002) and Read & Ponman (2003). This component can be removed using the so called blank field observations. De Luca & Molendi (2001) report some evidence for a secular evolution of the background level on a half year time scale. Therefore, background accumulations close to the date of the target observation are more suitable. In addition, variations in the instrumental background on a much shorter time scale have been seen (e.g. De Luca & Molendi 2001). Part of such periods with an increased background

**Table 2.** Parameters of the residual background models fitted in the 0.4–15 keV band. Col. (1): Cluster name. Cols. (2–4): Index of the “powerlaw/b” residual background model for MOS1, MOS2 and pn. Cols. (5–7): Normalization at 1 keV of the “powerlaw/b” residual background model scaled to 1 arcmin<sup>2</sup> area for MOS1, MOS2 and pn in units of  $10^{-4}$  cts s<sup>-1</sup> keV<sup>-1</sup> arcmin<sup>-2</sup>.

Cluster (RXCJ)	Index			Normalization		
	MOS1	MOS2	pn	MOS1	MOS2	pn
0014.3–3022	1.47	1.48	1.95	1.21	1.73	6.49
0043.4–2037	1.71	1.43	1.61	1.57	1.28	8.50
0232.2–4420	1.26	1.52	1.54	1.26	1.73	6.60
0307.0–2840	1.28	1.43	1.82	0.89	1.21	2.80
0528.9–3927	0.80	0.96	1.56	0.93	1.12	3.36
0532.9–3701	1.60	1.67	2.08	0.32	1.51	3.89
0658.5–5556	1.52	1.64	1.95	7.66	3.99	15.26
1131.9–1955	1.98	2.34	3.19	1.73	1.89	5.96
2337.6+0016	1.24	1.47	1.43	1.71	1.58	8.74

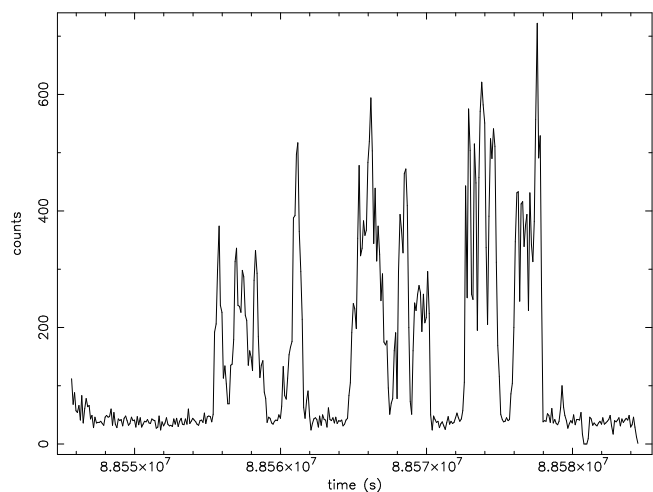


**Fig. 1.** pn light curve of RXCJ0658.5–5556 in the 10–15 keV energy band. Time is measured in second relative to the XMM-Newton internal clock.

are rejected through the analysis of the light curve (e.g. Read & Ponman 2003). However, we sometimes still observe a residual enhancement of the background associated with an increase in the quiet flux of soft protons. The typical time-scale for the variation of this ‘quiet’ component is comparable to or exceeds the typical observational time-scale. Therefore, it is in general not possible to remove observational intervals affected by this enhancement. Chen et al. (2003) describe an example of such an observation where quite different ‘quiet’ background levels are observed before and after a flare, respectively.

The photon background consists of foreground emission from the Galaxy as well as the Cosmic X-ray Background (CXB). Observations of the blank field also contain both components, provided the accumulations are done with the same instrumental set-up (e.g. with a particular filter) and the spectra of the X-ray background are the same for both the target and the blank field. This is only guaranteed for the CXB and the emission from the Galaxy halo. Since the Galaxy also plays a role as absorber and foreground emitter, it is important to have a similar absorbing column density for both the target and background accumulations. Additionally, there are some extra Galactic components, that display spatial variations. To constrain them, one has to look into the ROSAT All-Sky Survey data around both the background accumulations and the target. Observations with normal conditions of the Galactic emission are referred to the quiet Galactic zones. So are most of the X-ray background accumulations (Lumb et al. 2002; Read & Ponman 2003). Some source removal is performed on the existing background accumulations. This changes the shape and intensity of the residual CXB. Therefore, a similar source removal has to be performed in the analysis of the target.

Several available XMM-Newton pointings have been investigated. We conclude that the XMM-Newton pointings in the Chandra Deep Field South (CDFS) have similar background conditions as most targets and sufficient exposure time. Therefore, the CDFS is a good candidate for the background for our study. However, there is still a small difference between the background of our sources and the CDFS, e.g. the background ctr in the target observations is slightly higher (10–20%) than in the CDFS, which we ascribe mostly to the contamination by soft protons.

We have carefully planned this cluster study such that the radii in which the cluster emission can be observed extend up to spherical overdensities of 500, i.e., the ratio of the mean density of the dark halo with respect to the redshift-dependent critical density  $\rho_{\text{crit}}(z)$ . This is the region to which the cluster X-ray emission is expected to be essentially confined, covering about half of the field of view (FOV) of the XMM-Newton telescope. This enables us to extract a source spectrum from the background region of the target field for comparison with a background spectrum from the background field extracted with the same detector coordinates. Our residual background modeling procedure consists of analysing such regions not affected

by cluster emission. We assume little or no vignetting of the soft proton induced background, as suggested by recent studies (Lumb et al. 2002). Spectra are extracted from the 9.2–11.5’ region from the pointing center for our source observations and background candidate observations. In a first step, we compare the spectra extracted from the outer regions in the 0.4–15 keV band between the sources and the background pointings. The residual background signal found after the subtraction of the background field from the target field in this outer area is then modeled by a power law spectrum (model “powerlaw/b” in XSPEC, a power law background model which is convolved with the instrumental redistribution matrix but not with the effective area). We use this model to account for the excess soft proton background in our observations as compared to the background field. This residual power law background model is introduced over the whole energy range (“wabs\*mekal+powerlaw/b”, an emission spectrum from hot diffuse gas, e.g. Mewe et al. 1985, considering the Galactic absorption and modeling the residual background by a power law), which yields the correct shape of the background component after the combination with the blank field background (double background subtraction method). During this procedure, the normalization of the residual background component is always scaled to the area of the source extraction region.

In Fig. 2 we present examples of the residual background. The parameters of the residual background models fitted in the 0.4–15 keV band for the clusters are given in Table 2. The residual background in pn is higher than in MOS because the larger thickness of the pn-pixels leads to a higher sensitivity to the particle flux. Since the subtraction of the residual background is only a second order correction to the data and because of the large noise in the residual background data, we are not attempting a perfect model fitting, but approximating the data by a simple power law model. The uncertainty in the normalization is, anyway, within 5% and 10% for MOS and pn, respectively. The correction due to the residual background makes only a 1–4% effect in the cluster signals and an up to 10% effect to the temperature determinations for cluster radii  $r \leq 4'$ . At larger radii the effect of the correct background effect is large as shown in Fig. 3, but the uncertainty in the approximation of the residual background – a third order effect – is still small.

To recover the correct spectral shape and normalization of the cluster component, we need both the response matrix file (rmf) and auxiliary response file (arf). **The following need to be taken into account in either rmf or arf:** (i) **Pure redistribution matrix giving the probability that a photon of energy E, once detected, will be measured in data channel PI.** (ii) **Quantum efficiency (with closed filter position) of the CCD detector.** (iii) **Filter transmission.** (iv) **Geometric factors such as bad pixel corrections and gap corrections (around 4%).** (v) **Telescope effective area as a function of photon energy.** (vi) **Vignetting correction to effective area for off-axis**

pointings. We choose the `rmf` which corresponds to (i) and (ii) (with closed filter position). The pn `rmf` that corresponds to this choice has a ‘closed’ keyword in their naming conventions. For the MOS detectors we use software to generate such files, kindly provided by S. Sembay. **The `arf` corresponds to (iii), (iv) and (v) and is made according to the average flux detected in the different extraction annuli, which takes (vi) into account.** It is created using the XMM-SAS based program ‘`clarf`’ by A. Finoguenov. **Furthermore, in our analysis we apply the logarithmically spaced radial bins, which provide nearly the same flux per bin. The importance of the scattering due to the point-spread-function (PSF) is therefore suppressed. Using the XMM-Newton PSF calibrations by Ghizzardi (2001) we have estimated the loss fraction of the flux: 20% for the central bins ( $0.5'$ ) and less than 10% for the other bins ( $\geq 1'$ ) with energy dependent effects being negligible.**

In summary the spectral analysis is performed in two steps. (i) A model for the residual background (background difference) is obtained in XSPEC from a comparison of the outer region of the target and background fields (see Fig. 2 and Table 2). (ii) The spectral modeling is performed in XSPEC with the cluster region as source data, the CDFS as background and the residual background as a second model component with model parameters fixed to the values found in step (i) (see Fig. 5).

In Fig. 3 we present the temperature profiles resulting from this background subtraction method fitted in the 0.4–10 keV band for the example object, RXCJ0307.0–2840. We actually compare the results of the two step background subtraction considering the residual background with the simple one step background subtraction. In Fig. 4 we provide the comparisons of the results from MOS1, MOS2 and pn fitted in the 0.4–10 keV band. One notes that the residual background subtraction provides results in which all three instruments tend to show a slightly better consistency. The upper limit of the uncertainties between the instruments goes down from 90% to 15% after the residual background subtraction. A detailed treatment of the background does not completely remove the differences between the instruments. We found systematically lower temperatures obtained with pn compared to MOS1 and MOS2 (partially). Because the pn detector is sensitive to the soft component, the pn measurements are easily affected by the soft band, which results in the lower temperatures given by pn compared to MOS. Since the temperature estimates of the pn are more strongly dependent on the soft energy band compared to MOS, we have carried out a spectral analysis in the 1–10 keV band. Despite the larger error bars, all temperature determinations in the central three bins of the cluster become higher, once the 0.4–1 keV band is excluded. In the following we will systematically investigate the effect of an energy band selection in the temperature and mass estimate.

### 3. Results

#### 3.1. Redshift, mean temperature, and metallicity

In a first step of the data analysis we derive global properties of all nine galaxy clusters with good XMM-Newton data. Since a fraction of the clusters have cooling cores, dense central regions with lower temperature and so-called cooling flows, while the others do not display this phenomenon, we derive global temperatures including and excluding these regions. In addition the signal-to-noise decreases fast in the outer regions of the clusters. Therefore, the global temperature was determined in the  $r < 8'$  region and alternatively in the  $0.5 < r < 4'$  region (see Fig. 5). The global temperatures determined in both regions show some differences. The explanation is partially revealed by the temperature profiles. The metallicities in both zones are very similar.

After subtracting the background and applying the `rmf` and `arf`, we fit the spectra in XSPEC using the one and two step correction models (“`mekal*wabs`”, “`mekal*wabs+powerlaw/b`”). The fit using the latter model is better. For the regions covering radii of  $0.5 < r < 4'$  and  $r < 8'$ , respectively, we use the 0.4–10 keV and 1–10 keV energy bands. Furthermore, we exclude the regions of substructure and/or some very bright point sources for several clusters throughout the procedure (cf. Table 3). The temperature of the small and large substructures in the well-known post merger cluster RXCJ0658.5–5556 are  $8.3_{-1.4}^{+2.1}$  keV and  $15.0_{-1.9}^{+2.3}$  keV from the double background subtraction method in the 2–12 keV band. We exclude the small substructure to measure the global temperature. The flux within the region we excluded contributes 60% ( $10''$ ) to 85% ( $30''$ ) to the total flux of the point source. The **temperature** measurements vary within 10% after the subtraction.

The redshifts obtained from the X-ray data (see Table 4) which are ascribed to the ICM, are consistent with the redshifts obtained from optical spectra of individual cluster galaxies (see Böhringer et al. 2003) except for RXCJ2337.6+0016. The optical redshifts contain a heliocentric correction, while the uncertainty in the X-ray determined redshifts is one to two magnitude larger than this correction and thus no correction was made. We believe that the optical redshift of RXCJ2337.6+0016 with 5 coincident cluster galaxy redshifts is more reliable and accurate than the X-ray result at this stage. We plan to obtain further information on this object to resolve this discrepancy.

The measurements of the global temperatures are summarized in Table 4. Similar to the measurements for the  $0.5 < r < 4'$  region, the measurements for the  $r < 8'$  region in the 0.4–10 keV band are lower than in the 1–10 keV band. Therefore, we only provide the comparison of the measurements for the  $0.5 < r < 4'$  region fitted in two bands. The results obtained for the full and restricted spatial zones are consistent within  $1-2\sigma$  (formal errors) within 15% uncertainties.

The global temperatures obtained from model fits to the larger spectral range 0.4–10 keV are always lower compared to the temperatures obtained from 1–10 keV. To check if the discrepancy is partially due to residual Galactic emission, we undertake the following test. We extract the spectra from the inner (hereafter “A”) and outer (hereafter “B”) parts of the background region in both the background (hereafter “bkg”) and target (hereafter “src”) observations. If there is some difference in the Galactic emission between the background and target observations, there must be some residual Galactic emission after we subtract the spectrum “ $B(src) - B(bkg)$ ”, scaled by the area of the region A, from the spectrum “ $A(src) - A(bkg)$ ” because of the vignetting effect of the Galactic emission. We apply a thermal emission spectral model (“apec”) with all parameters free in XSPEC to fit this residual emission. We found that the temperature of this component is around 0.2 keV and the redshift is close to zero. In the following analysis, we fix the temperature to 0.2 keV, the abundance to solar abundance and the redshift to zero, and obtain the normalization of this component. We re-analyse the global properties of the clusters introducing the residual Galactic emission normalized by the area and vignetting effect. Since the difference in the temperatures determined in the 0.4–10 keV and 1–10 keV bands still remains, we report the temperature measurements setting the normalization of the residual Galactic emission to its upper limit (cf. Table 4). However, this component only makes a  $< 1\%$  effect in the cluster signals. It is thus clear that the discrepancy is not or not mainly due to the residual Galactic emission. This discrepancy will again be discussed below.

**Table 3.** Regions with substructures and point sources excluded from the analysis. Col. (1): Cluster name. Col. (2–3): Center of the circle in sky coordinates for J2000.0. Col. (4): Radii. Col. (5): “Yes” if there is an optical point-like counterpart in a digitized optical survey (e.g. DSS2).

Cluster (RXCJ)	$\alpha$ ( $^{\circ}$ )	$\delta$ ( $^{\circ}$ )	r ( $''$ )	opt
0014.3–3022	3.6306	−30.3754	15	Yes
	3.5198	−30.4154	15	Yes
	3.5172	−30.4176	10	Yes
	3.5353	−30.3654	30	
0232.2–4420	38.1566	−44.3634	20	Yes
0528.9–3927	82.2427	−39.4647	15	Yes
	82.3071	−39.4809	15	Yes
	82.1450	−39.3867	15	Yes
	82.1435	−39.3724	10	Yes
	82.1134	−39.3713	10	Yes
0532.9–3701	83.1957	−36.9415	15	
	83.1506	−37.0285	10	
0658.5–5556	104.5884	−55.9413	20	

### 3.1.1. Comparison with previous results

Mushotzky & Scharf (1997) have measured for RXCJ0014.3–3022 a temperature of  $12.08_{-0.88}^{+1.42}$  keV ( $2\sigma$  errors) with ASCA data. Horner (2001) presents the temperature for the same cluster of  $9.61_{-0.56}^{+0.64}$  keV, for RXCJ0232.2–4420 of  $7.19_{-0.38}^{+0.42}$  keV, for RXCJ0307.0–2840 of  $6.71_{-0.53}^{+0.60}$  keV, and for RXCJ1131.9–1955 of  $8.26_{-0.58}^{+0.63}$  keV, all with  $2\sigma$  errors based on ASCA data. Lemonon et al. (1997) measured a temperature for the post-merger cluster RXCJ1131.9–1955 of  $5 \pm 3$  keV using ROSAT PSPC data. They also found some evidence for a temperature gradient.

For the cluster RXCJ0658.5–5556 the published temperature measurements are less consistent. Tucker et al. (1998) measured a temperature of  $17.4 \pm 2.5$  keV ( $2\sigma$  error) with ASCA. Andreani et al. (1999) obtained  $14.5_{-1.7}^{+2.0}$  keV using both ASCA and ROSAT data. Yaqoob (1999) measured  $11 \sim 12$  keV with ASCA data. He found that a temperature of  $\sim 17$  keV can be artificially obtained if the true spectrum has a stronger low-energy cut-off than that for Galactic absorption only.

We notice that the ASCA spectra of RXCJ0658.5–5556 have in the 0.5–1 keV band only a few data points with large error bars. The differences in the temperature measurements described above come therefore clearly from the inclusion or exclusion of this soft part of the spectrum. Studies of nearby clusters suggest that putative non-thermal and warm thermal components are important at softer energies, while for rich clusters like Coma, the ICM dominates the X-ray emission up to 25 keV (Fusco-Femiano et al. 1999). Non-thermal emission dominates the emission at energies above 3 keV only in some of the groups of galaxies (Fukazawa et al. 2000). Since the expected temperatures of rich clusters are higher than 4 keV, we consider the temperature determination in the hard energy band as a more robust measure of the dominant gas mass component of a cluster, which traces the total mass. For RXCJ0658.5–5556 we decided to restrict our temperature determinations to the energy range 2–12 keV (see Tables 4 and 5).

Our results on RXCJ0658.5–5556 are consistent with Chandra measurements obtained by Markevitch et al. (2002) yielding a temperature of  $14.8_{-1.2}^{+1.7}$  keV from a fit of a spectrum extracted from the central  $r < 3'$  region. Although the authors show that  $k_B T > 15$  keV in some parts of this cluster, the temperatures have quite large error bars of 7 keV so that we regard this finding as not very significant.

Additionally, Markevitch et al. (2002) fixed the value of the galactic hydrogen column density to  $n_H = 4.6 \times 10^{20} \text{ cm}^{-2}$  which is significantly lower than  $n_H = 6.5 \times 10^{20} \text{ cm}^{-2}$  obtained from Dickey & Lockman (1999). To check this result with our XMM-Newton data we set all parameters to be free to fit the spectrum extracted from the annulus region covering radii of  $0.5 < r < 4'$  in the

0.4–12 keV band. In this case a high temperature of  $k_{\text{B}}T = 18.8 \pm 2.1$  keV was obtained while the  $n_{\text{H}}$  went down to an unrealistically small value of  $1.8 \pm 0.5 \times 10^{20} \text{ cm}^{-2}$ , although the remaining parameters were still relatively reasonable. Therefore, we decide to fix  $n_{\text{H}} = 6.5 \times 10^{20} \text{ cm}^{-2}$ , but exclude the soft band (0.4–2 keV). In this case we obtained stable results for the temperature, metallicity, and redshift (see Table 4). No significant metallicity gradients were found in our analysis.

We notice that the temperature of RXCJ0528.9–3927 (also in other clusters) changes significantly with the low cut-off of the energy band used in the fit. In Fig. 7, we thus used the X-ray spectra to test the energy band dependence and possible method dependencies by comparing the temperature measurements versus low energy band (low-E) cut-off from two different methods (the double background subtraction method and the method applied in Arnaud et al. 2002, i.e. we use the standard XMMSAS command ‘evigweight’ to correct vignetting, use ‘arfgem’ and ‘rmfgen’ to create on-axis arf and rmf, and apply the blank sky provided by Lumb 2002). For comparison, we applied the following models to fit the spectra in the 0.4–10 keV band after double background subtraction. We obtain  $k_{\text{B}}T = 7.69^{+0.28}_{-0.46}$  keV and  $n_{\text{H}} \sim 0 - 0.1 \times 10^{20} \text{ cm}^{-2}$  using a single-phase temperature model (“wabs\*mekal+powerlaw/b”) with free  $n_{\text{H}}$ . We obtain  $k_{\text{B}}T = 10.12 \pm 3.13$  keV using two component thermal model (“wabs\*(mekal+powerlaw)+powerlaw/b”) with fixed  $n_{\text{H}}$ . We also obtain  $k_{\text{B}}T_1 = 9.34^{+5.93}_{-1.04}$  keV and  $k_{\text{B}}T_2 \sim 0.49 - 1.34$  keV using two thermal component model (“wabs\*(mekal+apec)+powerlaw/b”), in which we fix the redshift of the soft component to the redshift of the cluster. The metallicity and redshift measurements among the different modelings and different low-E cut-off vary within 5%. The results presented in Fig. 7 suggest some influence of the low energy band on the temperature measurements. As we discussed above, the results obtained in the harder energy band should recover the correct cluster temperature. Similar phenomena are also found for A1413 (Pratt & Arnaud 2002) using XMM-Newton data, and Coma, A1795 and A3112 (Nevalainen et al. 2003) based on the comparison of XMM-Newton and ROSAT PSPC observations. Nevalainen et al. interpret this as a soft excess, possibly due to a ‘warm-hot’ intergalactic medium. We will analyse this feature of our sample in more detail in a forthcoming paper.

### 3.2. Temperature profiles

We have already noted that the differences between the global temperatures of the regions covering radii of  $0.5 < r < 4'$  and  $r < 8'$ , respectively, in Table 4 are possibly caused by systematic temperature gradients. For a more detailed study of the temperature profiles we divide the cluster regions into the five annuli 0–0.5', 0.5–1', 1–2', 2–4', and 4–8' (cf. Fig. 3). Note that in the spectra extracted from the outermost rings of RXCJ0014.3–3022

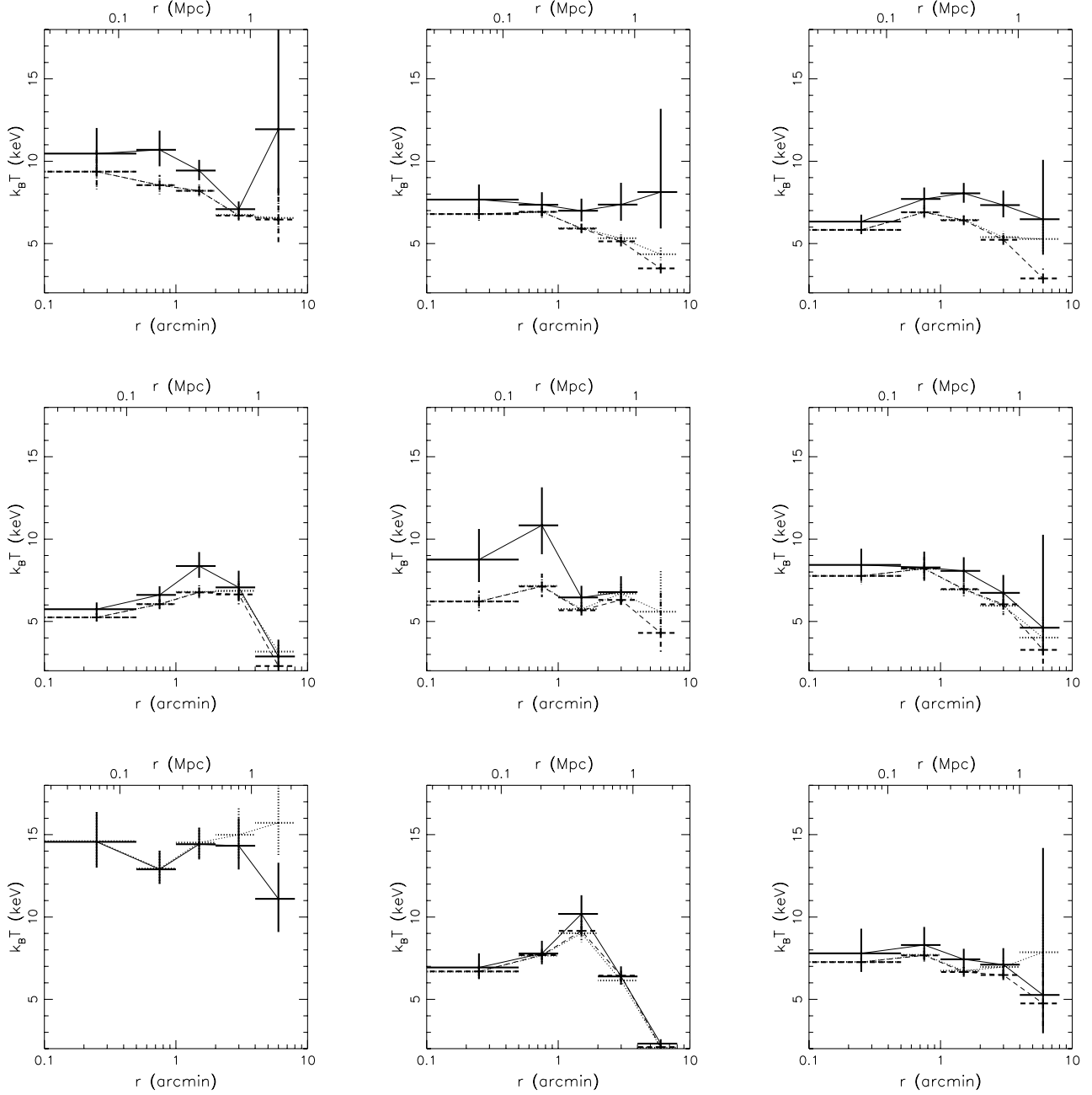
and RXCJ0528.9–3927 we ignore a narrow energy band containing the residual background around the 1.49 keV Al line (Freyberg et al. 2002).

Table 5 shows the temperature profile catalogue of the clusters from the spectral analysis fitted by one or two step background subtraction (“mekal\*wabs”, “mekal\*wabs+powerlaw/b”). We use both the  $> 0.4$  keV and  $> 1$  keV energy bands except for RXCJ0658.5–5556. We apply the 2–12 keV band for this high temperature cluster. The temperature profiles of the clusters are also shown in Fig. 6.

For most of the objects, the temperature can be measured out to  $r_{500}$ . The overall temperature profile is characterized by a rather moderate decrease towards the center, and a decrease towards the outer regions, yet on different levels, including no decrease at all for some of the clusters. This confirms a suggestion of Finoguenov et al. (2001b) that the differences in the behaviour of the temperature profiles in the outskirts of clusters have a statistical origin, rather than simple reflections of measurement errors.

To test the validity of the results without a geometrical deprojection in our analysis, we apply the deprojection model provided in XSPEC (“project”) to study the deprojection effect for RXCJ0307.0–2840. This model performs a three dimension to two dimension projection of shells onto annuli. It is assumed that the inner boundary is specified by the outer boundary of the next annulus in. In the “project” model, for each shell in a combined fit to all annuli spectra simultaneously, the contribution of each ellipsoidal shell to each annulus is determined and the spectral fitting results are then determined. In this fitting the outer shells are not affected by the emission from the inner shells. Similar work has been described by Pizzolato et al. (2003). Figure 8 presents the temperature profiles from the spectral fit with and without projected modeling in the 0.4–10 keV energy band. The temperature gradient becomes slightly more significant when the geometrical deprojection effect is taken into account. The differences are, however, within the error bars and can thus be neglected. The relatively small effect of the deprojection is due to the steep surface brightness profiles of clusters which strongly reduce the influence of the emission from the outer shells on the observed spectra of the central regions. Therefore, the application of deprojection gives really significant improvement only if the count statistics is very high (e.g. Matsushita et al. 2002).

Systematic differences in the temperature profiles caused by the inclusion of the 0.4–1 keV energy band in the spectral analysis are not the same among the clusters. Cluster RXCJ1131.9–1955 is not affected at all, RXCJ0014.3–3022, RXCJ0307.0–2840 and RXCJ0528.9–3927 are affected in the center, while RXCJ0043.4–2037 and RXCJ0232.2–4420 are affected in the outskirts. Since the instrumental setup used to observe this sample is the same, it hardly is an instrumental artifact. However, more detailed analyses are needed in order to distinguish between the Galactic and extragalac-



**Fig. 6.** From left to right and from top to bottom, temperature profiles of RXCJ0014.3–3022, RXCJ0043.4–2037, RXCJ0232.2–4420, RXCJ0307.0–2840, RXCJ0528.9–3927, RXCJ0532.9–3701, RXCJ0658.5–5556, RXCJ1131.9–1955 and RXCJ2337.6+0016. All the clusters except RXCJ0658.5–5556 are fitted in the 0.4–10 keV band with (dashed lines) and without (dotted lines) the residual background subtraction. And the solid lines present the case with the residual background subtraction but fitted in the 1–10 keV band. The corresponding lines show the temperature profiles. Temperature profiles of RXCJ0658.5–5556 are fitted in 2–12 keV with (solid lines) and without (dotted lines) the residual background subtraction.

tic origin of this component in the outskirts of some of the clusters in our sample (e.g. Finoguenov et al. 2003).

### 3.3. Modeling RXCJ0307.0–2840

We use RXCJ0307.0–2840 as an illustrative example to demonstrate the accuracy of measurements of the total gravitating cluster mass and the gas mass fraction attain-



**Table 4.** Global temperatures, metallicities and redshifts of REFLEX-DXL clusters. Col. (1): Cluster name. Col. (2): Radius of annulus in arcmin. Col. (3): Energy band for fit. Col. (4): X-ray temperature measurements. Col. (5): Metallicity in solar abundance. Col. (6): Redshift obtained from the X-ray spectrum. Col. (7):  $\chi^2$  per degree of freedom (d.o.f.). Col. (8): Redshift obtained from optical spectra as given in the REFLEX catalogue (see Böhringer et al. 2003). All X-ray spectra are fitted by the XSPEC model “mekal\*wabs+powerlaw/b”.

Cluster	Region	Energy band (keV)	$k_B T$ (keV)	$Z$ ( $Z_\odot$ )	$z_{X\text{-ray}}$	$\chi^2/d.o.f.$	$z_{\text{opt}}$
RXCJ0014.3-3022	$0 < r < 8'$	1 – 10	$8.65^{+0.43}_{-0.29}$	$0.24 \pm 0.05$	$0.294 \pm 0.008$	392.9/397	0.3066
	$0.5 < r < 4'$	0.4 – 10	$7.51^{+0.20}_{-0.21}$	$0.22 \pm 0.04$	$0.276 \pm 0.009$	383.2/371	
RXCJ0043.4-2037	$0 < r < 8'$	1 – 10	$7.63^{+0.21}_{-0.20}$	$0.22 \pm 0.04$	$0.274 \pm 0.007$	377.2/379	0.2924
	$0.5 < r < 4'$	0.4 – 10	$8.29^{+0.43}_{-0.32}$	$0.22 \pm 0.05$	$0.276 \pm 0.011$	269.4/258	
RXCJ0232.2-4420	$0 < r < 8'$	1 – 10	$7.50^{+0.47}_{-0.40}$	$0.23 \pm 0.06$	$0.309 \pm 0.015$	198.0/238	0.2836
	$0.5 < r < 4'$	0.4 – 10	$5.88^{+0.22}_{-0.21}$	$0.24 \pm 0.06$	$0.303 \pm 0.006$	197.8/197	
RXCJ0307.0-2840	$0 < r < 8'$	1 – 10	$5.96^{+0.23}_{-0.21}$	$0.25 \pm 0.06$	$0.302 \pm 0.011$	191.1/197	0.2578
	$0.5 < r < 4'$	0.4 – 10	$6.81^{+0.43}_{-0.39}$	$0.23 \pm 0.07$	$0.300 \pm 0.012$	124.4/129	
RXCJ0528.9-3927	$0 < r < 8'$	1 – 10	$6.70^{+0.24}_{-0.25}$	$0.32 \pm 0.05$	$0.275 \pm 0.002$	292.0/332	0.2839
	$0.5 < r < 4'$	0.4 – 10	$6.33^{+0.22}_{-0.17}$	$0.22 \pm 0.05$	$0.295 \pm 0.008$	384.2/287	
RXCJ0532.9-3701	$0 < r < 8'$	1 – 10	$6.27^{+0.20}_{-0.17}$	$0.23 \pm 0.05$	$0.296 \pm 0.010$	372.6/287	0.2747
	$0.5 < r < 4'$	0.4 – 10	$7.62^{+0.40}_{-0.33}$	$0.24 \pm 0.05$	$0.296 \pm 0.009$	195.4/195	
RXCJ0658-5557	$0 < r < 8'$	1 – 10	$6.17^{+0.24}_{-0.27}$	$0.28 \pm 0.06$	$0.241 \pm 0.002$	270.8/281	0.2965
	$0.5 < r < 4'$	0.4 – 10	$6.10^{+0.20}_{-0.22}$	$0.28 \pm 0.06$	$0.244 \pm 0.003$	275.0/251	
RXCJ1131.9-1955	$0 < r < 8'$	1 – 10	$6.17^{+0.21}_{-0.21}$	$0.28 \pm 0.06$	$0.244 \pm 0.004$	265.1/251	0.3075
	$0.5 < r < 4'$	0.4 – 10	$6.63^{+0.34}_{-0.31}$	$0.29 \pm 0.07$	$0.243 \pm 0.004$	176.5/167	
RXCJ2337.6+0016	$0 < r < 8'$	1 – 10	$8.07^{+0.59}_{-0.52}$	$0.31 \pm 0.08$	$0.262 \pm 0.012$	163.2/159	0.2779
	$0.5 < r < 4'$	0.4 – 10	$6.49^{+0.29}_{-0.27}$	$0.30 \pm 0.08$	$0.281 \pm 0.011$	162.8/148	
RXCJ2337.6+0016	$0 < r < 8'$	1 – 10	$6.42^{+0.28}_{-0.27}$	$0.31 \pm 0.08$	$0.281 \pm 0.010$	154.8/148	0.2965
	$0.5 < r < 4'$	0.4 – 10	$7.66^{+0.63}_{-0.52}$	$0.28 \pm 0.10$	$0.282 \pm 0.016$	91.5/97	
RXCJ2337.6+0016	$0 < r < 8'$	1 – 10	$7.46^{+0.38}_{-0.36}$	$0.34 \pm 0.07$	$0.274 \pm 0.003$	286.1/239	0.2965
	$0.5 < r < 4'$	0.4 – 10	$7.09^{+0.31}_{-0.44}$	$0.29 \pm 0.08$	$0.262 \pm 0.009$	226.5/202	
RXCJ2337.6+0016	$0 < r < 8'$	1 – 10	$6.98^{+0.35}_{-0.28}$	$0.30 \pm 0.09$	$0.262 \pm 0.011$	224.3/202	0.2965
	$0.5 < r < 4'$	0.4 – 10	$7.76^{+0.72}_{-0.48}$	$0.28 \pm 0.10$	$0.259 \pm 0.016$	143.7/137	
RXCJ2337.6+0016	$0 < r < 8'$	1 – 10	$13.59^{+0.71}_{-0.58}$	$0.24 \pm 0.03$	$0.287 \pm 0.002$	621.3/608	0.2965
	$0.5 < r < 4'$	0.4 – 10	$14.56^{+0.91}_{-0.69}$	$0.21 \pm 0.04$	$0.290 \pm 0.005$	378.1/400	
RXCJ2337.6+0016	$0 < r < 8'$	1 – 10	$14.61^{+0.57}_{-0.74}$	$0.21 \pm 0.04$	$0.291 \pm 0.004$	377.1/400	0.2965
	$0.5 < r < 4'$	0.4 – 10	$9.63^{+0.22}_{-0.17}$	$0.23 \pm 0.02$	$0.288 \pm 0.002$	1214.5/892	
RXCJ2337.6+0016	$0 < r < 8'$	1 – 10	$6.42^{+0.26}_{-0.25}$	$0.26 \pm 0.05$	$0.299 \pm 0.003$	322.5/283	0.3075
	$0.5 < r < 4'$	0.4 – 10	$6.71^{+0.08}_{-0.40}$	$0.23 \pm 0.09$	$0.285 \pm 0.009$	263.1/255	
RXCJ2337.6+0016	$0 < r < 8'$	1 – 10	$6.62^{+0.38}_{-0.21}$	$0.26 \pm 0.07$	$0.287 \pm 0.012$	248.4/255	0.2965
	$0.5 < r < 4'$	0.4 – 10	$7.44^{+0.67}_{-0.22}$	$0.26 \pm 0.07$	$0.295 \pm 0.024$	163.4/174	
RXCJ2337.6+0016	$0 < r < 8'$	1 – 10	$8.02^{+0.59}_{-0.57}$	$0.22 \pm 0.07$	$0.328 \pm 0.009$	211.1/255	0.2779
	$0.5 < r < 4'$	0.4 – 10	$6.77^{+0.29}_{-0.24}$	$0.24 \pm 0.06$	$0.315 \pm 0.011$	176.5/234	
RXCJ2337.6+0016	$0 < r < 8'$	1 – 10	$6.83^{+0.22}_{-0.28}$	$0.25 \pm 0.06$	$0.318 \pm 0.009$	172.7/234	0.2779
	$0.5 < r < 4'$	0.4 – 10	$7.50^{+0.44}_{-0.37}$	$0.22 \pm 0.06$	$0.317 \pm 0.011$	116.2/161	

\*Introduce the upper limit of the residual Galactic emission described by an “apec” model in the double background subtraction method.

able with the XMM-Newton observations of the REFLEX-DXL-like clusters. Similar analyses of the REFLEX-DXL clusters are in progress. RXCJ0307.0–2840 is also very bright, but at a slightly lower redshift than the selection range for the REFLEX-DXL clusters.

### 3.3.1. Gas distribution

The regularity of the photon distribution shown in Fig. 9 suggests that there are no large substructures in RXCJ0307.0–2840. We thus assume a radially symmetric gas distribution. In order to get the actual gas distribution we directly deproject the data from the spectroscopic

analysis to get the gas mass profile (cf. Fabian et al 1981; Kriss et al. 1983). We divide the rings used for the temperature determinations into small subrings and fit the normalization for each subring separately, fixing the temperature profile to the values obtained from the above spectral analysis, the metallicities to  $Z = 0.2Z_\odot$ , the redshifts to  $z_{\text{opt}}$  as given in Table 4, and the Galactic absorption to  $n_{\text{H}}$  as given in Table 1. We use a constant metallicity here since we did not detect a significant variation of metallicity with radius within the error limits of our analysis. In the soft band, the X-ray emission is almost independent of the temperature (Fabricant et al. 1980). The gas mass in each spherical shell is proportional to the square root

**Table 5.** Temperature profiles of REFLEX-DXL clusters obtained from the spectral analysis with residual background subtraction (double background subtraction) and without residual background subtraction. Col.(1): Cluster name. Col.(2): Energy band for spectral fit. Col.(3): Model used in XSPEC. Cols.(4-8): Temperature measurements. We do not obtain a consistent temperature measurement for RXCJ0528.9–3927 in 4–8' region from the combined data because of the high background.

Cluster	Energy band (keV)	Model	$k_B T$ (keV)				
			$0 < r < 0.5'$	$0.5 < r < 1'$	$1 < r < 2'$	$2 < r < 4'$	$4 < r < 8'$
RXCJ0014.3–3022	0.4-10	model1 <sup>a</sup>	$9.37^{+1.30}_{-1.07}$	$8.54^{+0.62}_{-0.54}$	$8.20^{+0.38}_{-0.35}$	$6.74^{+0.32}_{-0.29}$	$6.56^{+1.30}_{-1.02}$
		model2 <sup>b</sup>	$9.37^{+1.31}_{-1.07}$	$8.55^{+0.62}_{-0.55}$	$8.20^{+0.39}_{-0.35}$	$6.70^{+0.32}_{-0.30}$	$6.46^{+2.14}_{-1.49}$
RXCJ0043.4–2037	0.4-10	model2	$10.46^{+1.56}_{-1.33}$	$10.69^{+1.17}_{-1.00}$	$9.43^{+0.65}_{-0.59}$	$7.09^{+0.47}_{-0.43}$	$11.94^{+1.69}_{-4.03}$
		model1	$6.79^{+0.47}_{-0.41}$	$6.93^{+0.42}_{-0.37}$	$5.93^{+0.31}_{-0.28}$	$5.33^{+0.36}_{-0.34}$	$4.35^{+1.43}_{-0.37}$
RXCJ0232.2–4420	0.4-10	model2	$6.79^{+0.47}_{-0.42}$	$6.93^{+0.42}_{-0.37}$	$5.91^{+0.31}_{-0.28}$	$5.13^{+0.38}_{-0.34}$	$3.49^{+0.46}_{-0.35}$
		model1	$7.67^{+0.92}_{-0.76}$	$7.36^{+0.76}_{-0.66}$	$6.99^{+0.74}_{-0.65}$	$7.37^{+1.32}_{-0.99}$	$8.13^{+5.05}_{-2.21}$
RXCJ0307.0–2840	0.4-10	model2	$5.83^{+0.27}_{-0.25}$	$6.91^{+0.42}_{-0.37}$	$6.44^{+0.32}_{-0.29}$	$5.39^{+0.35}_{-0.34}$	$5.28^{+1.19}_{-0.61}$
		model1	$5.83^{+0.27}_{-0.25}$	$6.90^{+0.42}_{-0.37}$	$6.41^{+0.32}_{-0.30}$	$5.23^{+0.36}_{-0.33}$	$2.88^{+0.61}_{-0.37}$
RXCJ0307.0–2840	1.0-10	model2	$6.34^{+0.42}_{-0.37}$	$7.71^{+0.69}_{-0.60}$	$8.05^{+0.63}_{-0.57}$	$7.34^{+0.87}_{-0.74}$	$6.48^{+3.61}_{-2.16}$
		model1	$5.25^{+0.26}_{-0.24}$	$6.06^{+0.34}_{-0.31}$	$6.80^{+0.42}_{-0.39}$	$6.86^{+0.69}_{-0.61}$	$3.17^{+0.50}_{-0.40}$
RXCJ0528.9–3927	0.4-10	model2	$5.24^{+0.26}_{-0.24}$	$6.05^{+0.34}_{-0.31}$	$6.76^{+0.42}_{-0.39}$	$6.64^{+0.70}_{-0.60}$	$2.30^{+0.40}_{-0.30}$
		model1	$5.74^{+0.40}_{-0.36}$	$6.61^{+0.53}_{-0.46}$	$8.37^{+0.84}_{-0.72}$	$7.07^{+1.01}_{-0.84}$	$2.87^{+1.02}_{-0.63}$
RXCJ0528.9–3927	1.0-10	model2	$6.22^{+0.67}_{-0.58}$	$7.16^{+0.77}_{-0.65}$	$5.75^{+0.43}_{-0.38}$	$6.70^{+0.68}_{-0.58}$	$5.59^{+2.56}_{-1.58}$
		model1	$6.21^{+0.67}_{-0.58}$	$7.12^{+0.76}_{-0.64}$	$5.68^{+0.42}_{-0.37}$	$6.30^{+0.62}_{-0.53}$	$4.30^{+2.67}_{-1.14}$
RXCJ0532.9–3701	0.4-10	model2	$8.75^{+1.86}_{-1.36}$	$10.84^{+2.31}_{-1.76}$	$6.46^{+0.70}_{-0.59}$	$6.79^{+0.96}_{-0.77}$	
		model1	$7.77^{+0.61}_{-0.53}$	$8.19^{+0.70}_{-0.61}$	$6.93^{+0.48}_{-0.43}$	$5.96^{+0.64}_{-0.56}$	$4.02^{+1.24}_{-0.81}$
RXCJ0532.9–3701	1.0-10	model2	$7.77^{+0.61}_{-0.53}$	$8.21^{+0.71}_{-0.61}$	$6.96^{+0.49}_{-0.43}$	$6.04^{+0.69}_{-0.59}$	$3.28^{+1.34}_{-0.89}$
		model1	$8.44^{+0.98}_{-0.81}$	$8.28^{+0.97}_{-0.80}$	$8.07^{+0.83}_{-0.71}$	$6.73^{+1.09}_{-0.85}$	$4.61^{+5.65}_{-1.69}$
RXCJ0658.5–5556	2.0-12	model2	$14.60^{+1.81}_{-1.57}$	$12.94^{+1.13}_{-0.90}$	$14.52^{+0.98}_{-0.91}$	$14.99^{+1.62}_{-1.46}$	$15.72^{+2.40}_{-2.01}$
		model1	$14.57^{+1.57}_{-1.80}$	$12.90^{+1.11}_{-0.89}$	$14.42^{+0.98}_{-0.92}$	$14.33^{+1.68}_{-1.44}$	$11.1^{+2.20}_{-2.00}$
RXCJ1131.9–1955	0.4-10	model2	$6.69^{+0.46}_{-0.41}$	$7.66^{+0.47}_{-0.42}$	$9.02^{+0.61}_{-0.54}$	$6.15^{+0.36}_{-0.33}$	$2.06^{+0.11}_{-0.10}$
		model1	$6.70^{+0.47}_{-0.41}$	$7.69^{+0.47}_{-0.42}$	$9.15^{+0.63}_{-0.56}$	$6.44^{+0.41}_{-0.36}$	$2.10^{+0.14}_{-0.12}$
RXCJ2337.6+0016	1.0-10	model2	$6.93^{+0.86}_{-0.70}$	$7.79^{+0.77}_{-0.66}$	$10.19^{+1.14}_{-0.94}$	$6.39^{+0.61}_{-0.51}$	$2.31^{+0.27}_{-0.22}$
		model1	$7.27^{+0.67}_{-0.58}$	$7.70^{+0.48}_{-0.43}$	$6.73^{+0.31}_{-0.29}$	$6.96^{+0.53}_{-0.46}$	$7.86^{+2.34}_{-1.56}$
RXCJ2337.6+0016	0.4-10	model2	$7.26^{+0.68}_{-0.58}$	$7.67^{+0.48}_{-0.43}$	$6.66^{+0.31}_{-0.29}$	$6.48^{+0.49}_{-0.44}$	$4.75^{+2.52}_{-1.37}$
		model1	$7.80^{+1.49}_{-1.11}$	$8.30^{+1.09}_{-0.86}$	$7.43^{+0.64}_{-0.55}$	$7.11^{+1.00}_{-0.82}$	$5.26^{+8.93}_{-2.33}$

<sup>a</sup> mekal\*wabs.  
<sup>b</sup> mekal\*wabs+powerlaw/b.

of the integral emission, which can be calculated from the normalization of the spectroscopic analysis (e.g. Vikhlinin et al. 1999).

In Fig. 10 we show the electron number density profiles for RXCJ0307.0–2840. Here, 1 arcmin = 0.240 Mpc at  $z = 0.2578$ . For the fits we use the standard  $\beta$  model

$$n_e(r) = n_{e0} \left[ 1 + \left( \frac{r}{r_c} \right)^2 \right]^{-\frac{3\beta}{2}}, \quad (1)$$

with the core radius  $r_c$  and the shape parameter  $\beta$ . The parameters from the best  $\chi^2$  fits are listed in Table 6. The energy band used for the spectral fits does not affect the normalization, which corresponds to the electron number density profile (cf. Fig. 10).

### 3.3.2. Temperature distribution

The precise estimate of the temperature structure greatly contributes to a reliable mass distribution. The tempera-

ture profile of RXCJ0307.0–2840 drops towards the center due to cooling. We found that the parameterization

$$k_B T(r) = \frac{1}{Ar^2 + Br + C} \quad (2)$$

fits the measured temperature profiles quite well. Fig. 11 presents the best  $\chi^2$  fit for RXCJ0307.0–2840 with the parameters given in Table 6. The temperature profile in the outermost regions can be fitted by a polytropic model,  $k_B T(r) = k_B T_0 (n_e/n_{e0})^{\gamma-1}$  (e.g. Finoguenov et al. 2001b). In order for the system to be convectionally stable, the value of  $\gamma$  should not exceed  $5/3$ . Using the results of the spectral analysis in the 0.4–10 keV (1–10 keV) band we obtain  $\gamma = 1.59$  ( $\gamma = 1.46$ ), which fulfills the stability criteria.

### 3.3.3. Mass distribution

We assume the intracluster gas to be in hydrostatic equilibrium with the underlying gravitational potential domi-

nated by the dark matter component. For the cosmological constant  $\Lambda = 0$  we have

$$\frac{1}{\mu m_p n_e} \frac{d(n_e k_B T)}{dr} = -\frac{GM_{\text{DM}}(r)}{r^2}, \quad (3)$$

where  $n_e$  and  $k_B T$  are the electron number density and temperature distributions, respectively, and  $\mu = 0.62$  is the mean molecular weight per hydrogen atom (e.g. Zakamska & Narayan 2003).

Analytic models of the gas density and temperature profiles can be easily combined with Eq.(3) to obtain the mass profile:

$$M(< r) = \frac{r^2}{\mu m_p G} k_B T(r) \left[ \frac{3\beta r}{r_c^2 + r^2} + (2Ar + B) \right]. \quad (4)$$

We determine the mass distribution by using our temperature model and the  $\beta$  gas density model. We use a Mont-Carlo simulation to calculate the error bars.

Masses measured by the strong gravitational lensing are sometimes found to be larger compared to the measured masses based on X-rays (Böhringer et al. 2000; Wu 2000; Wu et al. 1998). High spatially resolved temperature profiles could help to resolve this discrepancy. In order to test the effects of temperature gradients we compare the mass estimates obtained under the assumptions of isothermality using the global temperature as measured in the  $0.5 < r < 4'$  region fitted in the 1–10 keV band, and of non-isothermality. The mass and gas mass profiles are plotted in Fig. 12. Under the assumption of hydrostatic equilibrium and isothermality, the virial radius and the total gravitational cluster mass are 2.14 Mpc and  $8.8 \times 10^{14} M_\odot$ , respectively.

### 3.3.4. Modeling a NFW mass distribution

Navarro et al. (1997; NFW) described a universal density profile from numerical simulations in hierarchical clustering scenarios,

$$\rho_{\text{DM}}(r) = \frac{\delta_{\text{crit}} \rho_{\text{crit}}}{(r/r_s)(1 + r/r_s)^2}, \quad (5)$$

where  $\delta_{\text{crit}}$  and  $r_s$  are the characteristic density and scale of the halo, respectively, and  $\rho_{\text{crit}}$ , the critical density of the universe at the cosmic epoch  $z$ .  $\delta_{\text{crit}}$  is related to the concentration parameter of a dark halo  $c = r_{\text{vir}}/r_s$  by

$$\delta_{\text{crit}} = \frac{200}{3} \frac{c^3}{\ln(1+c) - c/(1+c)}. \quad (6)$$

We fit the observational temperature profile to obtain the parameters  $\rho_s = \delta_{\text{crit}} \rho_{\text{crit}}$  and  $r_s$  if we assume that the hot gas is in hydrostatic equilibrium with the dark matter. The former is well fitted by a standard  $\beta$  profile. The parameters of the best fit of the NFW profile are presented in Table 6. The virial radius and virial mass estimates

are smaller than the estimates under the assumption of isothermality.

The NFW model describes the mass and gas mass fraction in the outer region well. Due to the cuspy NFW profile in the cluster center, the temperature fit based on the NFW model is higher than the observations. As a result, the gas mass fraction becomes lower in the center. But for this small central region we can not resolve the temperature structure well enough to perfectly recover the dark matter mass profile at the small radii.

### 3.3.5. Modified hydrostatic equilibrium with $\Lambda$

To be consistent with our background cosmological model with  $\Lambda \neq 0$  we should expect a second-order modification of the equation of hydrostatic equilibrium in the form

$$\frac{1}{\mu m_p n_e} \frac{d(n_e k_B T)}{dr} = -\frac{GM_{\text{DM}}(r)}{r^2} + \frac{\Lambda c^2}{3} r. \quad (7)$$

The effect of a non-zero  $\Lambda$  is smaller than one percent and can thus be neglected compared to the relative error in our mass estimations. Sussman & Hernandez (2003) also point out a small effect of  $\Lambda$  on virialized structures, and that it could be significant only in the linear regime on large scales of  $r \sim 30$  Mpc.

### 3.3.6. Gas mass fraction distribution

The distribution of the gas mass fraction is obtained according to the definition  $f_{\text{gas}}(r) = M_{\text{gas}}(r)/M_{\text{DM}}(r)$ . Since the derived gas mass is not completely unrelated to the derived total mass, we calculate the error bars of the gas fraction,  $\Delta f_{\text{gas}} = \sqrt{(\Delta M_{\text{gas}} M_{\text{DM}})^2 + (M_{\text{gas}} \Delta M_{\text{DM}})^2} / M_{\text{DM}}^2$ . The profile of the gas mass fraction based on the NFW modeling is steeper in the central region as seen in Fig. 13. In both mass modelings the gas fractions increase with radius, and range from  $f_{\text{gas}} = 0.035 \pm 0.012$  to  $0.138 \pm 0.026$  in the outermost regions ( $r_{\text{out}} = 1.441$  Mpc) (see Table 6).

These results are in good agreement with the measurements of Allen et al. (2002) based on Chandra observations of seven clusters yielding  $f_{\text{gas}} \sim 0.105$ – $0.138$ , and with the measurements of Sanderson et al. (2003) based on ASCA GIS & SIS and ROSAT/SPSP observations of 66 clusters yielding  $f_{\text{gas}} = 0.13 \pm 0.01 h_{70}^{-3/2}$ . Our value is below the universal baryon fraction obtained with the recent WMAP measurement  $f_b = \Omega_b/\Omega_m = 0.166$ , where  $\Omega_b h^2 = 0.0224$  and  $\Omega_m h^2 = 0.135$  (Spergel et al. 2003). This reassures the estimate of the mass distribution.

We also make use of the  $8 < r < 10'$  region to obtain an upper limit of the gas mass in this shell applying the model “mekal+wabs” without residual background subtraction. The upper limit of the total gas mass within 10 arcmin (2.37 Mpc) is  $2.49 \times 10^{14} M_\odot$ . Based on the above mass modeling described by Eq.(4), the upper limit of the gas fraction within 10 arcmin is 0.49. This unreasonably high value confirms that the background dominates in this region.

**Table 6.** Parameters of each model from the best  $\chi^2$  fits.  $r_{\text{out}} = 1.441$  Mpc is the outermost region where we can measure these parameters.  $r_{500}$  and  $r_{\text{vir}}$  are measured from the data.

Model	parameter	0.4–10 keV	1–10 keV
$\beta$	$r_c$ (Mpc)	$0.061 \pm 0.004$	$0.062 \pm 0.004$
	$n_{e0}$ ( $10^{-2} \text{cm}^{-3}$ )	$2.43 \pm 0.03$	$2.37 \pm 0.04$
	$\beta$	$0.60 \pm 0.02$	$0.60 \pm 0.02$
Eq.(2)	$A$ ( $\text{Mpc}^{-2} \text{keV}^{-1}$ )	$0.283 \pm 0.046$	$0.331 \pm 0.082$
	$B$ ( $\text{Mpc}^{-1} \text{keV}^{-1}$ )	$-0.240 \pm 0.028$	$-0.285 \pm 0.052$
	$C$ ( $\text{keV}^{-1}$ )	$0.195 \pm 0.004$	$0.181 \pm 0.007$
NFW	$r_s$ (Mpc)	$0.267 \pm 0.028$	$0.306 \pm 0.034$
	$\rho_s$ ( $10^{15} \text{M}_\odot \text{Mpc}^{-3}$ )	$2.2 \pm 0.3$	$1.9 \pm 0.5$
	$c$	$5.81 \pm 0.59$	$5.56 \pm 0.68$
	$M_{500}$ ( $10^{14} \text{M}_\odot$ )	$4.10 \pm 0.37$	$5.13 \pm 0.85$
	$r_{500}$ (Mpc)	1.038	1.116
	$M_{\text{vir}}$ ( $10^{14} \text{M}_\odot$ )	$5.52 \pm 0.49$	$7.13 \pm 1.18$
	$r_{\text{vir}}$ (Mpc)	1.550	1.701
	$f_{\text{gas}}(r < r_{\text{vir}})$	$0.144 \pm 0.028$	$0.124 \pm 0.036$
	$M_{r_{\text{out}}}$ ( $10^{14} \text{M}_\odot$ )	$5.17 \pm 0.46$	$6.30 \pm 1.04$
	$f_{\text{gas}}(r < r_{\text{out}})$	$0.138 \pm 0.026$	$0.112 \pm 0.032$
	Eq.(4)	$M_{500}$ ( $10^{14} \text{M}_\odot$ )	$6.86 \pm 0.01$
$r_{500}$ (Mpc)		1.231	1.118
$M_{r_{\text{out}}}$ ( $10^{14} \text{M}_\odot$ )		$6.91 \pm 0.01$	$16.46 \pm 4.69$
$f_{\text{gas}}(r < r_{\text{out}})$		$0.103 \pm 0.010$	$0.035 \pm 0.012$

#### 4. Summary and Conclusions

We studied eight clusters of the REFLEX-DXL sample, selected from the REFLEX cluster survey at redshifts around  $z \sim 0.3$ , and one supplementary cluster at redshift  $z = 0.2578$ . The data are from the MOS1, MOS2 and pn detectors of XMM-Newton. The consistent results from the three detectors, obtained by excluding the energies below 1 keV, give a good confidence in the applied method and provide tight constraints on the ICM parameters like the temperature, metallicity, and redshift.

Some of the clusters have been previously studied with ASCA, ROSAT and Chandra. The Chandra measurement of the temperature of RXCJ0658.5–5556 includes mainly the central  $r < 3'$  region, where the temperature is high. We measure the global temperatures over a larger radial range  $0.5 < r < 4'$  and  $r < 8'$ , respectively.

The parameter which best characterizes cluster mass, and which is most relevant for studies of the LSS and cosmology, is the hot temperature of the bulk of the ICM. To avoid contamination by a possible central cooling core and by a possible soft excess or residual calibration uncertainties, we excluded the central  $r < 0.5'$  region and the softest part of the X-ray spectrum ( $< 1$  keV) yielding reliable temperatures. These are the global temperatures that will be used in Paper I to derive the X-ray temperature function for this sample.

We obtained the spatially resolved X-ray temperature profiles for each cluster. For the determination of temperature profiles, the good statistics of the data allowed us to derive temperature values in five radial bins. In the inner regions an accuracy of better than 10–20 % can still be reached while the errors increase in the outer or out-

ermost two bins. The temperature varies as a function of radius by factors of 1.5–2. The intracluster gas is cool in the center of RXCJ0232.2–4420, RXCJ0307.0–2840, RXCJ0528.9–3927, and RXCJ1131.9–1955. No significant cooling gas is found with temperatures below 2 keV. In the outer region, the temperature drops at different levels. The differences of the temperature profiles in the cluster center may reveal that some clusters have relaxed cooling cores (but not all) and to some degree that we see the effect of non-gravitational processes. In this respect, it is remarkable that cooling cores are not only found in clusters with symmetric and regular X-ray images which might suggest a relaxed dynamical state, but also in the elongated, very disturbed cluster RXCJ1131.9–1955.

To study RXCJ0307.0–2840 in detail, we find a model which fits the complex temperature profile of this cluster quite well.

The mass distribution of this cluster, based on the precise measurements of the distributions of the temperature and gas density, is similar to the mass distribution obtained under the assumption of isothermality within the region we can measure. We investigated the gas mass fraction of RXCJ0307.0–2840 and found an increasing gas mass fraction as a function of radius, which is typical for most clusters. In the outermost region of the cluster, it is below the value of the universal baryon fraction. The uncertainty of the gas fraction is mainly caused by the temperature measurement. Therefore, a reliable determination of the temperature profile is a key point to obtain the precise estimates of both the mass and the gas mass fraction. It plays an important role in the M-T scaling relation.

*Acknowledgements.* The XMM-Newton project is supported by the Bundesministerium für Bildung und Forschung, Deutschen Zentrum für Luft und Raumfahrt (BMBF/DLR), the Max-Planck Society and the Haidenhaim-Stiftung. We acknowledge Jacqueline Bergeron, PI of the XMM-Newton observation of the CDFS, and Martin Turner, PI of the XMM-Newton observation of RXJ0658.5-5556. We acknowledge Steve Sembay who kindly provides us the software to generate the *rmf* for MOS and Wolfgang Pietsch, Michael Freyberg, Frank Haberl and Ulrich G. Briel providing useful suggestions. YYZ acknowledges receiving the International Max-Planck Research School Fellowship. AF acknowledges receiving the Max-Planck-Gesellschaft Fellowship. PS acknowledges support under the DLR grant No. 50 OR 9708 35. YYZ thanks Linda Pittroff for careful reading the manuscript and useful suggestions.

## References

- Allen, S. W., Schmidt, R. W., & Fabian, A. C., 2002, *MNRAS*, 334, L11
- Andreani, P., Böhringer, H., dall'Oglio, G., et al., 1999, *ApJ*, 513, 23
- Arnaud, M., Majerowicz, S., Lumb, D., et al., 2002, *A&A*, 390, 27
- Böhringer, H., Soucail, G., Mellier, Y., Ikebe, Y., & Schuecker, P., 2000, *A&A*, 353, 124
- Böhringer, H., Schuecker, P., Guzzo, L., et al., 2001a, *A&A*, 369, 826
- Böhringer, H., Schuecker, P., Lynam, P., et al., 2001b, *Msngr*, 106, 24
- Böhringer, H., Schuecker, P., Zhang, Y.-Y., et al., 2003, *A&A*, to be submitted (Paper I)
- Cavaliere, A., & Fusco-Femiano, R., 1976, *A&A*, 49, 137
- Chen, Y., Ikebe, I., & Böhringer, H., 2003, preprint, *A&A*, submitted
- De Luca, A. & Molendi, S., 2001, in *Symp. New Visions of the X-ray Universe in the XMM-Newton and Chandra Era* ( Noordwijk: ESA), in press
- Dickey, J. M., & Lockman, F. J., 1990, *ARA&A*, 28, 215
- Ettori, S., De Grandi, S., & Molendi, S., 2002, *A&A*, 391, 841
- Evrard, A. E., 1997, *MNRAS*, 292, 289
- Fabian, A. C., Hu, E. M., Cowie, L. L., Grindlay, J., 1981, *ApJ*, 248, 47
- Fabricant, D., Lecar, M., & Gorenstein, P., 1980, *ApJ*, 241, 552
- Finoguenov, A., Arnaud, M., & David, L. P., 2001a, *ApJ*, 555, 191
- Finoguenov, A., Reiprich, T. H., & Böhringer, H., 2001b, *A&A*, 368, 749
- Finoguenov, A., Jones, C., Böhringer, H., & Ponman, T. J., 2002, *ApJ*, 578, 74
- Finoguenov, A., Briel, U. G., & Henry, J. P., 2003, *A&A*, accepted, preprint [astro-ph/0309019]
- Freyberg, M. J., Pfeffermann, E., & Briel, U. G., 2001, in *Symp. New Visions of the X-ray Universe in the XMM-Newton and Chandra Era* ( Noordwijk: ESA), in press
- Fukazawa, Y., Makishima, K., Tamura, T., et al., 2000, *MNRAS*, 313, 21
- Fusco-Femiano, R., dal Fiume, D., Feretti, L., et al., 1999, *ApJ*, 513, L21
- Ghizzardi, S., 2001, In-flight calibration of the PSF for the MOS1 and MOS2 cameras, EPIC-MCT-TN-011 (Internal report)
- Horner, H., 2001, Ph.D. thesis, X-ray Scaling Laws for Galaxy Clusters and Groups
- Kriss, G. A., Cioffi, D. F., Canizares, C. R., 1983, *ApJ*, 272, 439
- Lemonon, L., Pierre, M., Hunstead, R., et al., 1997, *A&A*, 326, 34
- Lumb, D. H., Warwick, R. S., Page, M., & De Luca, A., 2002, *A&A*, 389, 93
- Markevitch, M., Forman, W. R., Sarazin, C. L., & Vikhlinin, A., 1998, *ApJ*, 503, 77
- Markevitch, M., Gonzalez, A. H., David, L., et al., 2002, *ApJ*, 567, L27
- Matsushita, K., Belsole, E., Finoguenov, A., & Böhringer, H., 2002, *A&A*, 386, 77
- Mewe, R., Gronenschild, E. H. B. M., & van den Oord, G. H. J., 1985, *A&AS*, 62, 197
- Molendi, S., & De Grandi, S., 1999, *A&A*, 351, L41
- Mushotzky, R. F. & Scharf, C. A., 1997, *ApJ*, 482, L13
- Navarro, J. F., Frenk, C. S., & White, S. D. M., 1997, *ApJ*, 490, 493 (NFW)
- Nevalainen, J., Lieu, R., Bonamente, M., & Lumb, D., 2003, *ApJ*, 584, 716
- Pizzolato, F., Molendi, S., Ghizzardi, S., & De Grandi, S., 2003, *ApJ*, 592, 62
- Ponman, T. J., Sanderson, A. J. R., & Finoguenov, A., 2003, *MNRAS*, 343, 331
- Pratt, G. W., & Arnaud, M., 2002, *A&A*, 394, 375
- Randall, S. W., Sarazin, C. L., & Ricker, P. M., 2002, *AAS*, 201, 6706
- Read, A. M., 2002, preprint [astro-ph/0212436]
- Read, A. M., & Ponman, T. J., 2003, *A&A*, accepted, preprint [astro-ph/0304147]
- Sanderson, A. J. R., Ponman, T. J., Finoguenov, A., Lloyd-Davies, E. J., Markevitch, M., 2003, *MNRAS*, 340, 989
- Schuecker, P., Böhringer, H., Collins, C. A., & Guzzo, L., 2003, *A&A*, 398, 867
- Serio, S., Peres, G., Vaiana, G. S., Golub, L., & Rosner, R., 1981, *ApJ*, 243, 288
- Spergel, D. N., Verde, L., Peiris, H. V., et al., 2003, *ApJS*, 148, 175
- Sussman, R. A., & Hernandez, X., 2003, *MNRAS*, accepted, preprint [astro-ph/0304385]
- Tucker, W., Blanco, P., Rappoport, S., et al., 1998, *ApJ*, 496, L5
- Vikhlinin, A., Forman, W., & Jones, C., 1999, *ApJ*, 525, 47
- Vikhlinin, A., VanSpeybroeck, L., Markevitch, M., Forman, W. R., & Grego, L., 2002, *ApJ*, 578, L107
- Voit, G. M., & Bryan, G. L., 2001, *Nature*, 414, 425

- Voit, G. M., Bryan, G. L., Balogh, M. L., & Bower, R. G., 2002, *ApJ*, 576, 601  
 White, D. A., 2000, *MNRAS*, 312, 663  
 White, S. D. M., Navarro, J. F., Evrard, A. E., & Frenk, C. S., 1993, *Nature*, 366, 429  
 Wu, X.-P., Chiueh, T., Fang, L.-Z., & Xue, Y.-J., 1998, *MNRAS*, 301, 861  
 Wu, X.-P., 2000, *MNRAS*, 316, 299  
 Yaqoob, T., 1999, *ApJ*, 511, L75  
 Zakamska, N. L., & Narayan, R., 2003, *ApJ*, 582, 162  
 Zhang, Y.-Y., & Wu, X.-P., 2003, *ApJ*, 583, 529

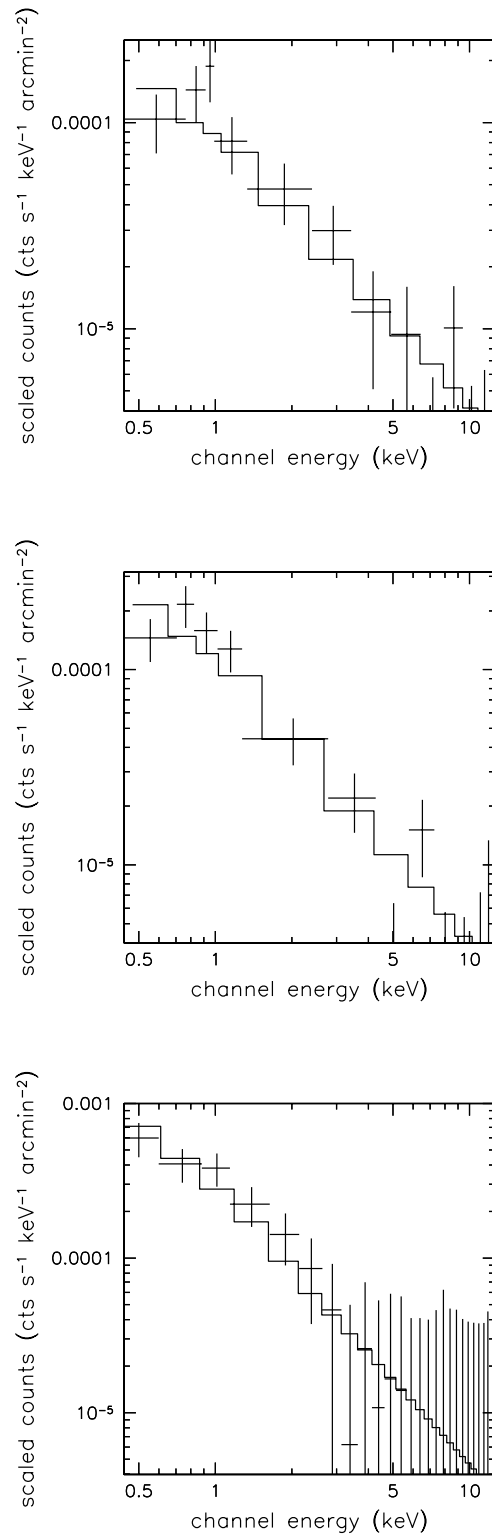


**Fig. 2.** Residual background (after subtraction of the background obtained from the XMM-Newton observations of CDFS) of RXCJ0307.0–2840 for the 9.2–11.5' region from the pointing centers of the MOS1 (top), MOS2 (middle) and pn (bottom) scaled to 1 arcmin<sup>2</sup> area. The data are fitted by a power law model (solid lines).

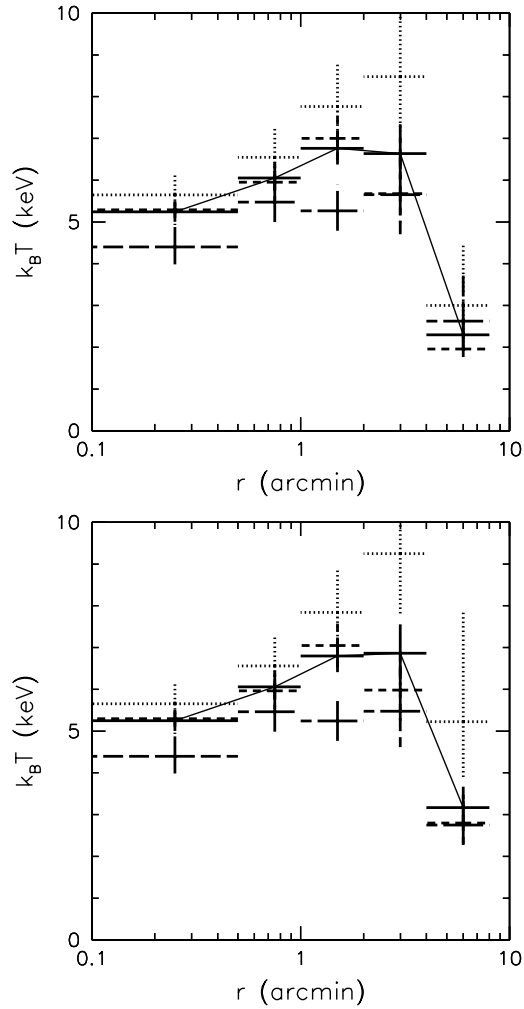


**Fig. 3.** Temperature profiles for RXCJ0307.0–2840 with residual background subtraction (upper panel) and without residual background subtraction (lower panel) fitted in the 0.4–10 keV band for MOS1 data (dotted lines), MOS2 data (dashed lines), pn data (dash-dotted lines) and combined data (solid lines). Additional solid lines connect the temperature measurements for the combined data.

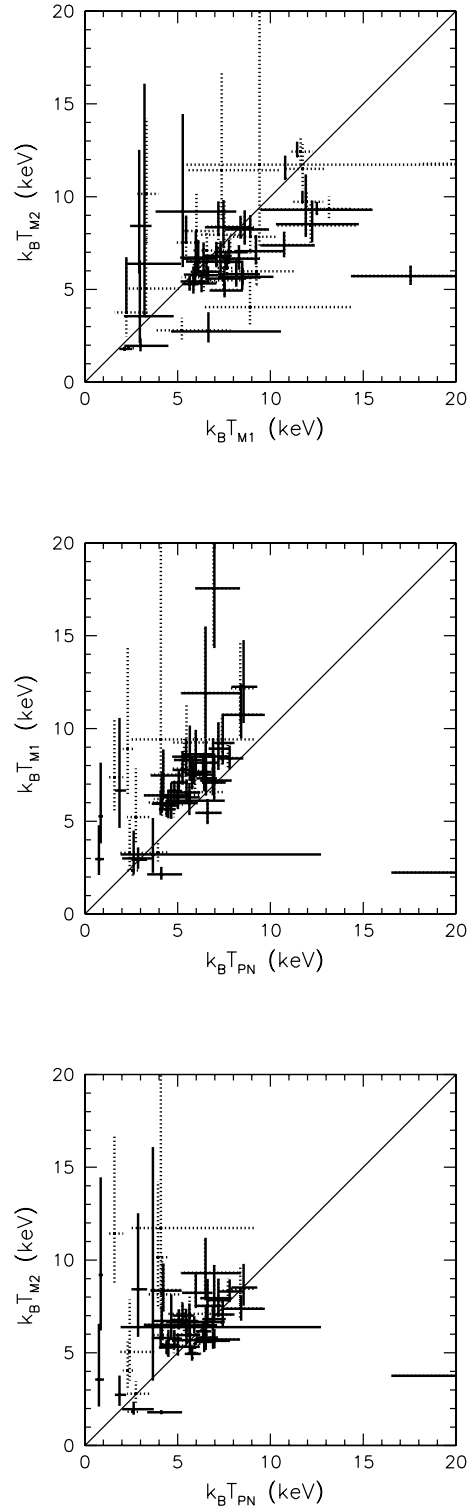


**Fig. 4.** Comparison of the temperature estimates for RXCJ0014.3–3022, RXCJ0043.4–2037, RXCJ0232.2–4420, RXCJ0307.0–2840, RXCJ0528.9–3927, RXCJ0532.9–3701, RXCJ0658.5–5556, RXCJ1131.9–1955 and RXCJ2337.6+0016 from MOS1, MOS2 and pn fitted in the 0.4–10 keV band with residual background subtraction (solid lines) and without residual background subtraction (dotted lines).

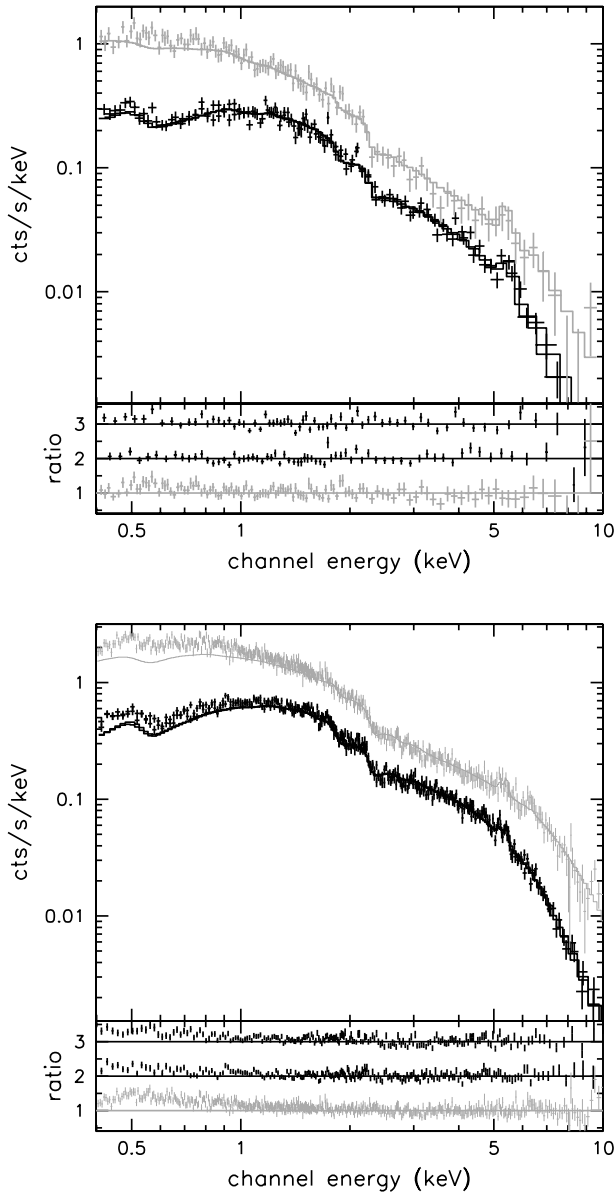


**Fig. 5.** XMM-Newton spectra of RXCJ0307.0–2840 (top panel, fitted in the 1–10 keV band) and RXCJ0658.5–5556 (bottom panel, fitted in the 2–12 keV band) extracted from the  $0.5 < r < 4'$  region (pn in grey and MOS in black) with mekal model, considering the Galactic absorption and modeling the residual background by a power law. The ratios of the observational data to the models are in the lower parts of the panels (offset zero for pn, +1 for MOS1, +2 for MOS2).

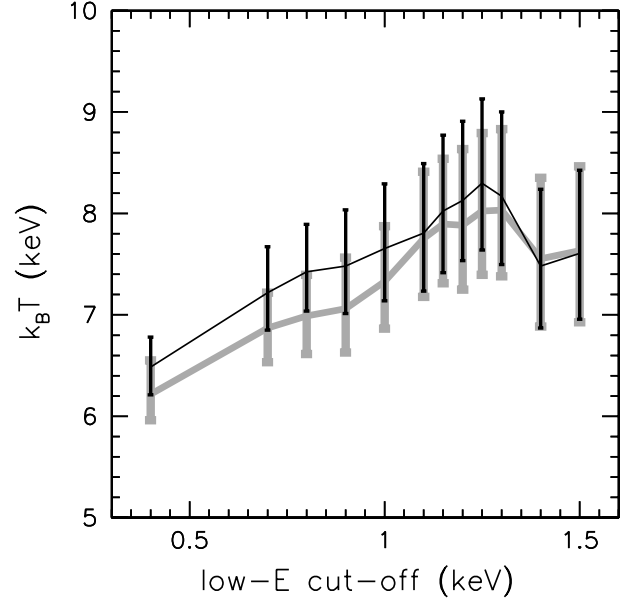


**Fig. 7.** The temperature measurements versus low-E cut-off from two different methods, the double background subtraction method (black) and the method applied in Arnaud et al. 2002 (grey).

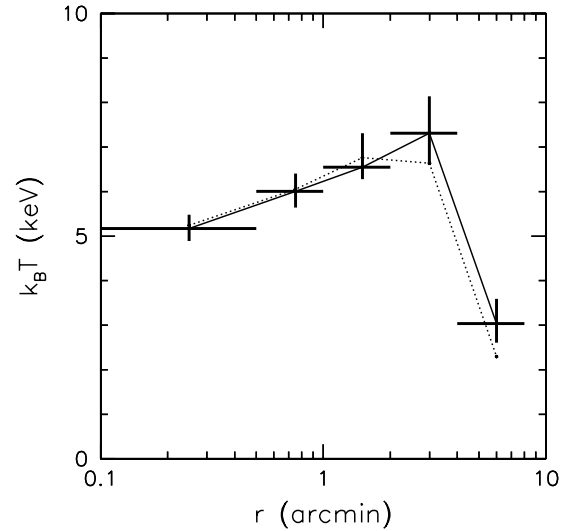


**Fig. 8.** Temperature profiles for RXCJ0307.0–2840 from spectral fits with (solid lines) and without (dashed lines) a geometrical deprojection.



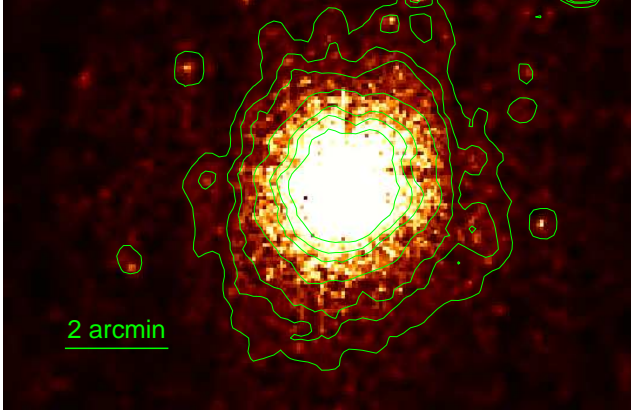


**Fig. 9.** Merged image from the three instruments for RXCJ0307.0–2840 in the 0.5–2 keV band. Superposed contours suggest a quite regular morphology.

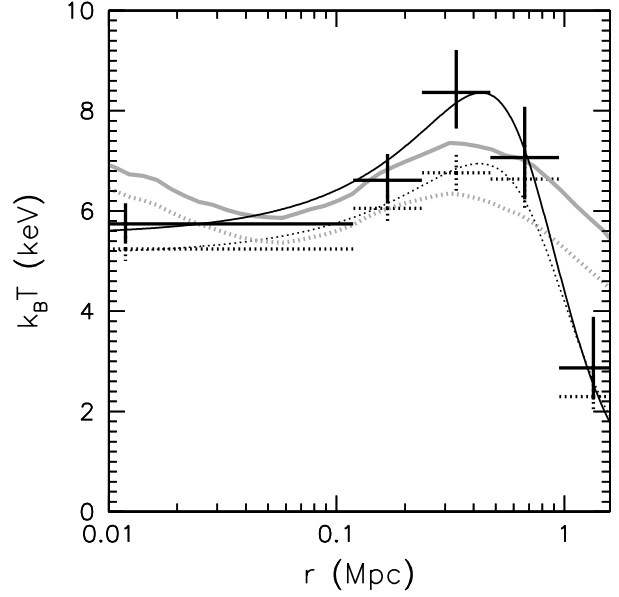


**Fig. 11.** Measured temperatures of RXCJ0307.0–2840 fitted in the 0.4–10 keV band (dotted lines) and 1–10 keV band (solid lines). The corresponding curves show the best fits using the NFW profile (grey) and Eq.(2) (black).

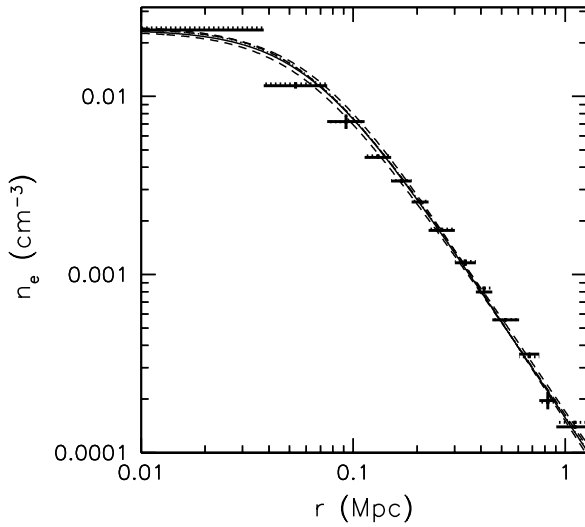


**Fig. 10.** Measured electron number density profiles of RXCJ0307.0–2840 fitted in the 0.4–10 keV band (dotted lines) and 1–10 keV band (solid lines), respectively. The corresponding curves present the best fits using the standard  $\beta$  model with the confidence intervals (dashed curves).

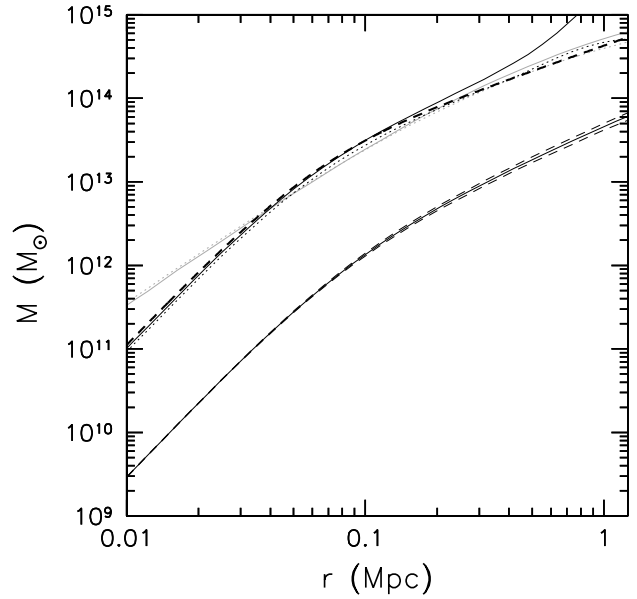


**Fig. 12.** Mass profiles (top) for RXCJ0307.0–2840 based on the temperature measurements fitted in the 0.4–10 keV band (dotted curves) and 1–10 keV band (solid curves) using the NFW model (grey) and Eq.(4) (black). An additional dashed curve presents the mass profile under the assumption of isothermality. The solid curve (bottom) with the confidence intervals (dashed curves) presents the gas mass distribution.

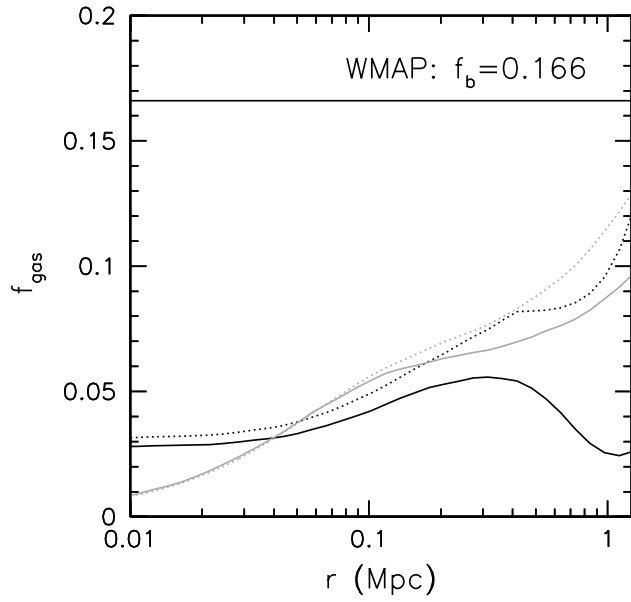


**Fig. 13.** Gas mass fraction distributions based on the temperature measurements fitted in the 0.4–10 keV band (dotted curves) and 1–10 keV band (solid curves) using the NFW model (grey) and Eq.(4) (black).